

An optical transient candidate of \lesssim 2-second duration captured by wide-field video observations

Noriaki ARIMA,^{1,2,*} Mamoru DOI,^{2,3} Shigeyuki SAKO,^{2,4,5} Yuu NIINO,⁶ Ryou OHSAWA,^{3,7} Nozomu TOMINAGA,^{3,7,8} Masaomi TANAKA,⁹ Michael RICHMOND,¹⁰ Shinsuke ABE,¹ Naoto KOBAYASHI,⁶ Sohei KONDO,⁶ Yuki MORI,⁶ Ko ARIMATSU,^{11,12} Toshihiro KASUGA,^{3,13} Shin-ichiro OKUMURA,¹⁴ Jun-ichi WATANABE,^{3,7} and Takuya YAMASHITA³

¹Department of Aerospace Engineering, Nihon University, 7-24-1 Narashinodai, Funabashi, Chiba, 274-8501, Japan

²Institute of Astronomy, Graduate School of Science, The University of Tokyo, 2-21-1 Osawa, Mitaka, Tokyo 181-0015, Japan

³National Astronomical Observatory of Japan, National Institutes of Natural Sciences, 2-21-1 Osawa, Mitaka, Tokyo 181-8588, Japan

⁴UTokyo Organization for Planetary Space Science, The University of Tokyo, 7-3-1 Hongo, Bunkyo-ku, Tokyo 113-0033, Japan

⁵Collaborative Research Organization for Space Science and Technology, The University of Tokyo, 7-3-1 Hongo, Bunkyo-ku, Tokyo 113-0033, Japan

⁶Kiso Observatory, Institute of Astronomy, Graduate School of Science, The University of Tokyo, 10762-30 Mitake, Kiso-machi, Kiso-gun, Nagano 397-0101, Japan

⁷Astronomical Science Program, Graduate Institute for Advanced Studies, SOKENDAI 2-21-1 Osawa, Mitaka, Tokyo 181-8588, Japan

⁸Department of Physics, Faculty of Science and Engineering, Konan University, 8-9-1 Okamoto, Kobe, Hyogo 658-8501, Japan

⁹Astronomical Institute, Tohoku University, Sendai 980-8578, Japan

¹⁰Physics Department, Rochester Institute of Technology, 84 Lomb Memorial Drive, Rochester, NY 14623, USA

¹¹Astronomical Observatory, Graduate School of Science, Kyoto University, Kitashirakawa-oiwake-cho, Sakyo-ku, Kyoto, Kyoto 606-8502, Japan

¹²Ishigakijima Astronomical Observatory, 1024-1, Arakawa, Ishigaki, Okinawa, 907-0024, Japan

¹³Nishi-Harima Astronomical Observatory, Center for Astronomy, University of Hyogo, 407-2, Nishigaichi, Sayo, Hyogo, 679-5313, Japan

¹⁴Japan Spaceguard Association, Bisei Spaceguard Center, 1716-3 Okura, Bisei, Ibara, Okayama 714-1411, Japan

*E-mail: arima.noriaki@nihon-u.ac.jp

ORCID: 0000-0002-2721-7109, 0000-0002-8792-2205, 0000-0001-5322-5076, 0000-0001-5797-6010, 0000-0001-8253-6850, 0000-0001-8537-3153, 0000-0002-6247-4979, 0000-0003-4578-2619, 0000-0003-1260-9502, 0000-0001-5903-7391, 0000-0002-1873-3494, 0000-0003-4391-4446

Abstract

Recent time-domain surveys in the optical have revealed rapid transients that evolve on timescales of $\lesssim 10$ days, expanding the population of transients toward the short-duration regime. The transient search on even shorter timescales, particularly those lasting only seconds, or less, remains a largely unexplored frontier, offering the significant potential for discovering objects from unexpected populations. Very short-duration optical transients could be potential counterparts to millisecond-duration fast radio bursts (FRBs), providing clues about their origins. However, the optical search for transients on such short timescales has been limited primarily due to instrumental constraints. Here we report the discovery of an optical transient candidate (TMG20200322) with a duration of $\lesssim 2$ s by wide-field video observations in the direction of the Earth's shadow. TMG20200322 was detected in just two consecutive images of 1-second exposure time, with its shape becoming elongated in the second frame. PSF shape variability analysis of the field stars reveals such an elongated PSF cannot be explained by atmospheric fluctuations. We investigate the potential origins of TMG20200322 in two scenarios: meteoroid impact flashes on near-Earth asteroids (NEAs) and head-on meteors in the Earth's atmosphere. None of the scenarios provides a satisfactory explanation for this transient. We derive a sky-projected rate of the TMG20200322 event to be $R_{\text{trans}} = (3.4 \times 10^{-2})^{+0.13}_{-0.028} \text{ deg}^{-2} \text{ day}^{-1}$ and an upper limit of second-timescale transients with durations of $1 \text{ s} \leq \tau \leq 15 \text{ s}$ to be $R_{\text{trans}} \lesssim 0.10 \text{ deg}^{-2} \text{ day}^{-1}$ for the non-detection case. We highlight that continuous monitoring observations in the direction of the Earth's shadow could be a key strategy to unveiling a new population of optical transients on timescales of seconds or less.

Keywords: methods: observational — methods: data analysis

1 Introduction

In recent years, time-domain sky surveys have dramatically expanded our ability to detect and classify transients of various kinds. By visiting the same field once every few days or less, high-cadence optical surveys such as All-Sky Automated Survey for

Supernovae (ASAS-SN; Shappee et al. 2014), the Asteroid Terrestrial-impact Last Alert System (ATLAS; Tonry et al. 2018; Smith et al. 2020), the The Panoramic Survey Telescope and Rapid Response System (Pan-STARRS; Chambers et al. 2016) and the Zwicky Transient Facility (ZTF; Bellm et al. 2019) have led to the identification of a diverse set of rapidly evolving transients. These

* Corresponding author. Email: arima.noriaki@nihon-u.ac.jp

rapid transients can reach peak luminosities comparable or even exceeding those of typical supernovae, yet their thermal emission that evolves on much shorter ($\lesssim 10$ days) timescales (e.g., Drout et al. 2014; Arcavi et al. 2016; Prentice et al. 2018; Ho et al. 2020). The Vera C. Rubin Observatory's Legacy Survey of Space and Time (LSST; Ivezić et al. 2019), which will soon begin science operations, will reveal the dynamic sky by discovering millions of transient phenomena nightly.

The discovery of new populations of transients often occurs serendipitously when exploring new regions of observational parameter space. Gamma-ray bursts (GRBs) are now recognized as γ -ray transients with durations ranging from sub-seconds to hundreds of seconds and powered by relativistic jets of extragalactic origin (Meegan et al. 1992). GRBs were first discovered in the late 1960s by the military Vela satellites, which were originally designed to monitor γ -rays associated with nuclear explosions in outer space (Klebesadel et al. 1973). A handful of observations have successfully detected the prompt optical emission for some GRBs (e.g., Vestrand et al. 2005; Racusin et al. 2008). A millisecond-duration radio pulse—now known as a fast radio burst (FRB)—was first identified in archival 1.4 GHz radio pulsar survey data and reported in 2007 (Lorimer et al. 2007). Although FRBs are now widely recognized as a new class of extragalactic radio transients, their origin and physical mechanisms responsible for the brief, high-energy radio emission are not well understood (Thornton et al. 2013; Petroff et al. 2016; Platts et al. 2019). So far, no extragalactic optical transient counterparts to FRBs have been identified, with the only exception of the X-ray burst from the Galactic magnetar SGR J1935+2154, which was associated with FRB 200428 (Bochenek et al. 2020; Li et al. 2021).

Continuous imaging of the same sky region allows us to search for transient phenomena on the shortest timescale, set by the exposure time of individual frames. Berger et al. (2013) searched for fast optical transients with durations as short as approximately 33 minutes by the Pan-STARRS Medium-Deep Survey using consecutive two photometric g , r -bands. Although several flare events of Galactic M-dwarf stars were detected, no plausible fast extragalactic transients were found. With the non-detection result, they placed an upper limit on the sky-projected event rate of extragalactic fast transients at $\lesssim 22.5$ mag of $R(\tau = 33 \text{ min}) \lesssim 0.12 \text{ deg}^{-2} \text{ day}^{-1}$. With detectable timescales of 1.2 minutes and limiting magnitude of $m_g \sim 23$ mag, Andreoni et al. (2020) conducted a multi-wavelength (from γ -rays to radio bands) transient search for the primary purpose of discovering optical counterparts to FRBs. Nine candidates were discovered in the program, all of which were classified as probably stellar flares on the basis of their multiband images and follow-up observations, giving an upper limit of the event rate of transients of $R(\tau = 1.2 \text{ min}) \lesssim 1.6 \text{ deg}^{-2} \text{ day}^{-1}$.

The parameter space of optical transients lasting a few seconds or less remains largely unexplored. To date, only a handful of optical surveys have systematically attempted to probe timescales of a few seconds or shorter, and very few have simultaneously achieved both moderate sensitivity and a wide field of view (FoV). The typical readout time of CCDs, on the order of ~ 10 seconds, constitutes one of the major limitations in probing the second-timescale regime. As a result, our understanding of the occurrence rates and spatial distributions of optical phenomena on timescales of a few seconds or less remains limited. In particular, models such as the magnetar flare scenario for FRBs predict optical flashes lasting less than one second (Yang et al. 2019; Chen et al. 2020; Beloborodov 2020), yet remain observationally elusive. The “Pi of the Sky”

project (Sokołowski et al. 2010) performed a transient search with a timescale of $\gtrsim 10$ seconds and a depth of 11 mag, giving an all-sky upper limit of transients brighter than 11 mag is < 300 per day. For ultra-fast ($\ll 1$ s) time domain searches, Tingay & Joubert (2021) performed observations with dual small camera systems (diameter of $\lesssim 10$ cm) and an exposure time of 21 ms, reaching a limiting magnitude of $mv \sim 6.6$. From this, they derived an upper limit to the transient event rate of $0.8 \text{ deg}^{-2} \text{ day}^{-1}$.

Previous optical observations with high temporal resolution reported that glints of sunlight reflected from artificial satellites and space debris are significant contaminant in searching for short-duration transients, most of which are located in low Earth orbit (LEO; altitude of $\leq 2,000$ km) and geostationary orbit (GEO; $\sim 36,000$ km above the equator) (e.g., Corbett et al. 2020; Nir et al. 2021a; Nir et al. 2021b; Tanaka et al. 2025). Richmond et al. (2020) and the following Arimatsu et al. (2021) conducted searches for “optical flashes” including expected optical emission from FRBs by monitoring video imaging with wide-field CMOS imagers to explore timescales of $1.5 - 11.5$ s and $0.1 - 1.3$ s, respectively. Their transient search programs subsequently focused on the Earth’s shadow region at GEO, where contamination from sunlight glints by man-made objects is minimized. Their non-detection results placed upper limits on the event rates of optical transients of $R(\tau = 1.5 - 11.5 \text{ s}) \lesssim 1.46 \text{ deg}^{-2} \text{ day}^{-1}$ and $R(\tau = 0.1 - 1.3 \text{ s}) \lesssim 9.1 \text{ deg}^{-2} \text{ day}^{-1}$, respectively.

In this work, we conduct a systematic search for transients lasting as short as one second using consecutive 1-frame per second (1 fps) video observations targeting the Earth’s shadow region by Tomo-e Gozen, which is described in Section 2. In Section 3, we describe our transient-detection pipeline that identifies point sources with durations as short as one second in a series of 1 fps data cubes. We present the discovery of a flash-like transient candidate, TMG20200322, with a duration of $\lesssim 2$ s in Section 4, and we discuss the possible origin of this transient in Section 5. The derived event rate of second-timescale optical transients by comparing previous studies is also described.

2 Observations

We carry out observations using the Tomo-e Gozen camera mounted on the 105 cm Schmidt telescope at the Kiso Observatory in Japan. Tomo-e Gozen is a wide-field mosaic CMOS camera that consists of 84 CMOS image sensors (Sako et al. 2018). Each CMOS sensor has 2000×1128 photosensitive pixels of size $19 \mu\text{m}$ on a side with a pixel scale of $1.189 \text{ arcsec/pixel}$, which corresponds to a total FoV of 20.8 deg^2 ($39'.7 \times 22'.4$ for each sensor). Tomo-e Gozen is capable of video imaging at up to 2 fps in full-frame readout mode. In normal operation, no optical filters are used (only a glass window is attached). The wavelength coverage of Tomo-e Gozen spans approximately $370 - 730 \text{ nm}$, with a peak quantum efficiency of 0.68 at $\lambda = 500 \text{ nm}$ (Kojima et al. 2018).

Observations are conducted on 28 nights between 20 November 2019 and 25 March 2020. Semi-automatic observations are performed during lunar ages 0–9 and 21–29.5 days, when the Earth’s shadow region is visible at elevations $\gtrsim 30$ deg. This lunar phase constraint is geometrically necessary, as the Earth’s shadow (antisolar) direction coincides with the Moon’s position during full moon. We operate Tomo-e Gozen in 1 fps mode (with an exposure time of 1.0 s), conducting up to 30 consecutive pointings (approximately one hour) at fixed sky coordinates. To ensure the FoV of Tomo-e Gozen ($\phi \sim 9$ deg) remained within the Earth’s shadow at GEO throughout the night, we apply telescope dithering to the cen-

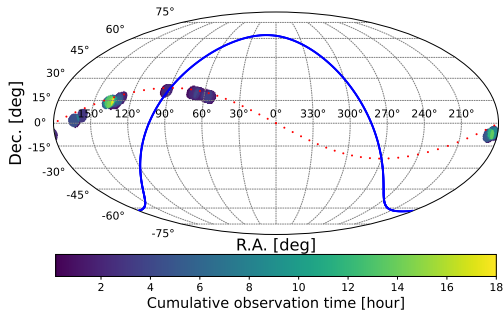


Fig. 1. Survey footprint of our 1 fps video observations targeting Earth's shadow regions at GEO. Each pointing area is shown as a circle with a diameter of $\phi = 9$ deg, corresponding to the FoV of Tomo-e Gozen. The cumulative observation time in hours is color-coded. The blue solid curve denotes the Galactic plane, while the red dotted curve marks the Ecliptic plane. Alt text: All-sky map in equatorial coordinates showing the coverage of our survey.

ter of the Earth's shadow approximately once per hour. Each video data cube generated from all 84 CMOS sensors of Tomo-e Gozen consists of 120 frames per sensor and has a data size of approximately 1.1 GB. In total, we obtain approximately 50 hours of 1-fps video data cubes with data size of ~ 135 TB. This translates to an areal exposure — the product of the total observed sky area and total observation time — of approximately $790 \text{ deg}^2 \cdot \text{hour}^1$, which is about 16 times greater than the previous work by Richmond et al. (2020) which used the prototype model of Tomo-e Gozen ($\sim 50 \text{ deg}^2 \cdot \text{hour}$). Figure 1 shows the footprint of our Earth's shadow observations. Overlapping regions with longer exposure times are visible, resulting from shifting the pointing center.

Raw images obtained by the Tomo-e Gozen camera are automatically reduced via the Tomo-e Gozen analysis servers (Sako et al. 2018), where basic reduction processing of dark frame subtraction and flat-field correction are performed. For the reduced images, astrometric calibration is performed employing the *Gaia* DR2 catalog (epoch: 2015.5) (Gaia Collaboration et al. 2018) using Astrometry.net software (Lang et al. 2010). We use the reduced and astrometrically calibrated frame images in our analysis. We derive the photometric zero points of the Tomo-e Gozen images by using the *Gaia* DR2 *G*-band photometric system (Gaia Collaboration et al. 2018). We calculate the photometric zero point by cross-matching sources on each frame image of Tomo-e Gozen with *Gaia* DR2 catalog sources whose magnitude ranges $12 \leq m_G \leq 16$ mag using the VizieR database service (Ochsenbein et al. 2000). Color correction is not performed in our analysis. We omit airmass correction because we perform relative photometry for sources within the same image. Figure 2 presents a histogram of the limiting magnitudes of our video frame images. We exclude frame images with limiting magnitudes shallower than $m_G = 16$ mag for the following transient search. The median value is 17.48 mag (signal-to-noise ratio $S/N = 5$), which we adopt as the limiting magnitude of this work.

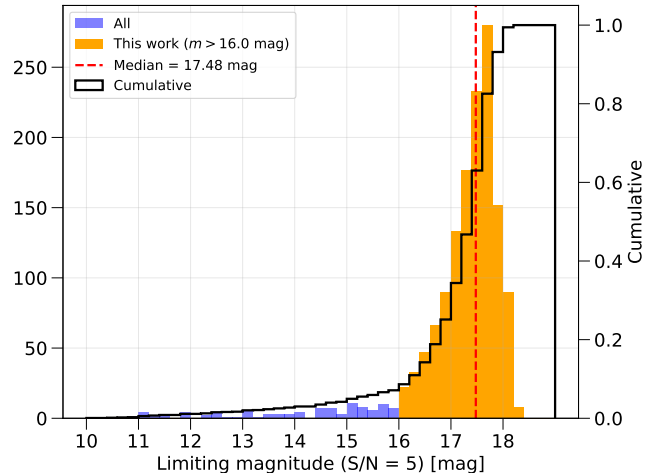


Fig. 2. Histogram of the limiting magnitudes for our 1 fps video observations. The limiting magnitude is derived from each data cube consisting of 120 frames, using CMOS sensor ID 133, which has median sensitivity among the 84 sensors. The red vertical line indicates the median limiting magnitude ($S/N = 5$), which is 17.48 mag. The black curve represents the cumulative distribution of the histogram, corresponding to the right vertical axis. For the transient search analysis described below, we set a limiting magnitude cut at $m_{\text{lim}} = 16.0$ mag and exclude frames with shallower limiting magnitudes. The binning interval is 0.2 mag. Alt text: A graph of histograms with a reference line.

3 Search for second-timescale transients

3.1 Transient detection

To search for second-timescale transients from video data, we developed a custom transient-detection pipeline. The flowchart of our pipeline is shown in Figure 3. In the left part of the flowchart, the input data cube consisting of 120 frames is stacked along the time axis to generate a single, deep image. The stacked image serves as a reference for stationary, non-transient objects. We adopt median stacking to ensure that transient events appearing in only a few frames are excluded from the stacked image. Our pipeline is capable of detecting transient events with durations as short as one second from the 120-frame data cube (See Section 5 for more details). The stacked images are then background-subtracted and source detection is performed using the SEP package (Barbary 2016), a Python wrapper of SExtractor (Bertin & Arnouts 1996). At the same time, a segmentation map of the same size as the stacked image, hereafter referred to as “segmap”, is generated. In the segmap, the pixel coordinates of the detected objects are recorded along with their corresponding identification numbers². For each stacked image, an average point spread function (PSF) is modeled using bright stars by fitting a 2D Gaussian function and incorporating the residuals of the fit (observed brightness of the stellar profile) using PythonPhot (Jones et al. 2015), a Python wrapper of the core functions of DAOPHOT (Stetson 1987).

In the right part of the flowchart, source detection is performed on each background-subtracted frame by convolving with the PSF model generated from the stacked image with the detection threshold of 1σ of the sky-background noise. Aperture photometry is then carried out for each detected object using two fixed aperture radii of 3 and 5 pixels (approximately 3.6 and 6.0 arcseconds, respectively). Sources detected in each frame image are classified

¹ Note that the areal exposure is calculated after removing the shallow-depth data ($m_{\text{lim}} > 16$ mag) and masked pixels in our transient search. See Section 3 for more details.

² A segmentation map can optionally be generated during the source detection process with SEP.

into two categories based on the corresponding segmap:

- i. masked objects, which are detected in the median stack image
- ii. unmasked objects, which are only detected in frame images

Figure 4 illustrates how to search transient events in our pipeline. Objects with duplicate segmap IDs are excluded during this process. We only use the unmasked objects for the following transient selection. This reduces the total areal exposure of our transient search, which is taken into account for the event rate calculation in Section 5.

3.2 Selection criteria

To reduce false positives from unmasked objects, we employ a classification diagram based on the parameter $\text{peak}/\sqrt{\text{npix}}$, ratio of the peak count and square root of the number of pixels (npix) and the peak count derived on the model-PSF-convolved image (cpeak). The use of using these parameters is based on the previous work aimed at classifying stars and galaxies (Yamagata & Maehara 1986). This diagram reflects the brightness profile of astronomical objects and is effective in distinguishing between stars and non-stellar objects. Objects with large peak and small npix values – such as cosmic ray hits and electrical noise – are located above the star sequence in Figure 3. For extended objects, such as galaxies (masked objects) and meteors (unmasked objects) with large npix and moderate peak values are located under the star sequence. We use an empirically derived boundary to select point sources from unmasked objects as shown in Figure 3. We further limit unmasked objects with ellipticity $e < 0.5$ defined as $e = 1 - b/a$, where a and b are the semi-major and semi-minor axes of an object. Transient candidates that meet the selection criteria described above are finally visually inspected. We also cross-match with Pan-STARRS DR1 sources via the VizieR database service (Ochsenbein et al. 2000) using a search radius of $r_{\text{PS1}} = 2.0$ arcseconds to identify potential optical counterparts.

4 Results

4.1 Source classification

In the analysis described above, 392 events pass our selection criteria. We classify candidate sources into several categories based on the shape, time variations of positions and brightness on the subsequent frame images. The categories we used for source classification are as follows.

1. Transient candidate
2. Moving object
3. Meteor
4. Electronical defect
5. Cosmic ray
6. transient caused by clouds
7. Image deviation
8. Positional offset of stars
9. Bad pixel (including hot/cold pixel)
10. Spider pattern by bright stars

Moving objects include asteroids in the solar system and may also include artificial satellites or space debris orbiting outside GEO in Earth's shadow observations. We separate the category of moving objects and meteors in terms of their apparent shapes, i.e. point sources and elongated ones. The other categories of (4 - 10) are false positives caused by external factors or instrumental problems. We visually inspect the moving images of each candidate event and

find one possible transient candidate.

4.2 A candidate of second-timescale transients

The transient candidate TMG20200322 is detected on the image taken on 22 March 2020 at 15:02:25.043 UT. The discovery coordinates are $(\text{RA}, \text{Dec})_{\text{J2000.0}} = (12^{\text{h}} 18^{\text{m}} 31^{\text{s}}.6, -4^{\circ} 55' 07''.5)$ and its Galactic coordinates are $(l, b) = (287.76391, 56.98059)$ in degrees. We present a light curve derived from forced photometry at the coordinates of TMG20200322 in Figure 5. TMG20200322 has a $\text{S}/\text{N} \sim 10.2$ and ~ 12.4 for the 1st and 2nd frames measured by aperture photometry with a radius of 6 arcsec. The corresponding *Gaia* *G*-band magnitude is $m_G = 16.89 \pm 0.11$ mag and 16.65 ± 0.09 mag for the first and second detection frames, respectively (Table 1). We compare the light curve of TMG20200322 with those of the field stars on the same image in Figure 6. The light curves of reference stars show no systematic variations in frames 108 and 109, confirming that the observed brightening is intrinsic to the transient source.

In Figure 7, we show zoomed-in image cutouts of the two detection frames of TMG20200322. We find a variation in the spatial brightness distribution between the two frames. Specifically, the second frame image exhibits a directional elongation toward the northeast. The semi-major axis measured at an isophotal level of 1σ of the background rms is 4.27 arcsec, corresponding to a significance of 6.1σ relative to the distribution of the field stars (Fig. 8). TMG20200322 also exhibits significantly higher ellipticity in the second frame ($e = 0.50 \pm 0.05$) compared to those of the field stars, although the first frame has typical value ($e = 0.16 \pm 0.13$). The flux barycenter between the two frames differs by ~ 4.5 arcsec, which is significant given the seeing condition (~ 3 arcsec) and the pixel scale of the Tomo-e Gozen camera (1.189 arcsec/pixel). On the other hand, the peak pixel positions in the two frames are nearly identical, which differs by just one pixel (see Table 1). This suggests that TMG20200322 could be a stationary object showing an extended component in its brightness distribution.

Since our observations target the Earth's shadow region at GEO, reflections from artificial objects within the shadow are unlikely to be detected. However, the possibility of reflections from objects located outside the GEO region cannot be entirely excluded. We obtain a list of cataloged artificial objects within a radius of 5 degrees of the coordinates of TMG20200322 at the time of discovery using the Space Track database³. The coordinates of TMG20200322 and the Earth's shadow region at the time of discovery are shown in Figure 9. For TMG20200322 to move out of the Earth's shadow region, its physical distance would need to be about 3 times that of GEO ($\gtrsim 100,000$ km). The most distant cataloged object ("CZ-3B DEB") is 46,427 km from the Earth's surface. Therefore, it is unlikely that TMG20200322 is a cataloged artificial object. If we assume that TMG20200322 is an object illuminated by reflected sunlight at 100,000 km from Earth, its characteristic diameter would range from 0.5 to 1.4 m depending on the albedo values assumed (0.1 and 0.85). However, the physical size estimated from the elongation in the second frame is ~ 4.5 km, which contradicts the size derived from the observed magnitude. This discrepancy indicates that the assumption that TMG20200322 is an artificial object reflecting sunlight is unlikely.

No host galaxy candidates or point source counterparts for TMG20200322 are detected in the Tomo-e Gozen stacked image. We investigate the Pan-STARRS1 (PS1) 3π survey source catalog (limiting magnitude of $m_{\text{lim}} \sim 23$ mag in the r_{PS1} band)

³ <https://www.SpaceTrack.org/>

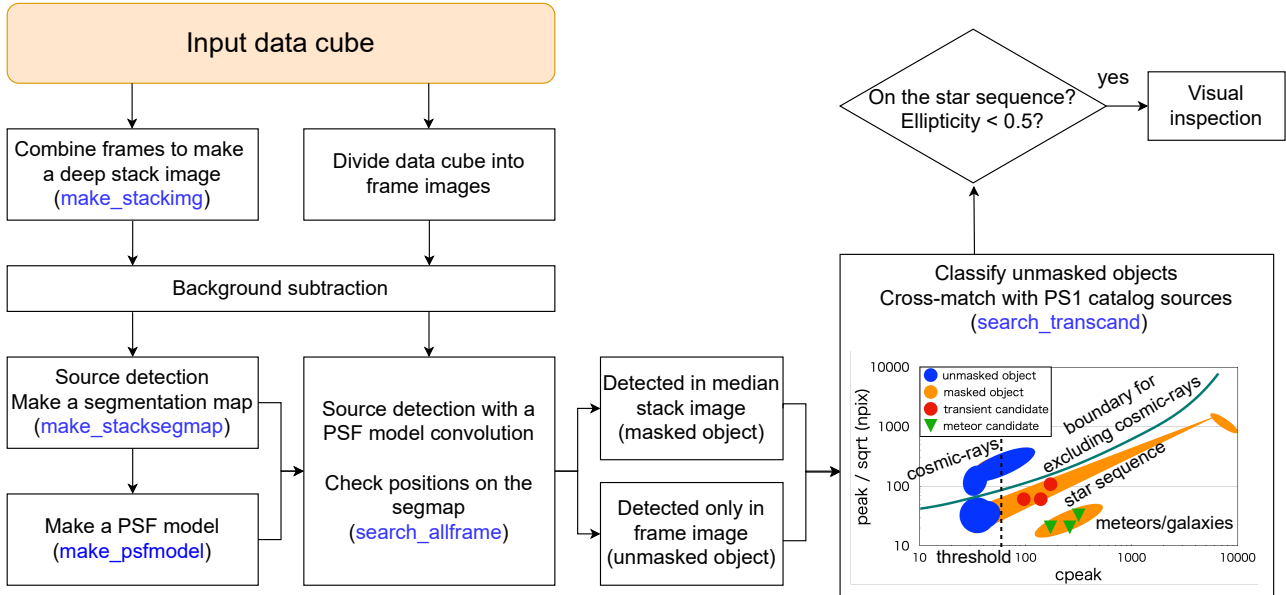


Fig. 3. Flowchart of our transient detection pipeline. The input data cube is processed through two analytical flows: the stacking process (core functions `make_stackimg`, `make_stacksegmap` and `make_psfmodel` shown as blue in the brackets) and per-frame processing (`search_allframe`). Objects detected in individual frames are compared against a binary image called a segmentation map (`segmap`), which contains positional information of detected objects in the stacked image. Unmasked objects are those that are detected only in some frames but are not detected in the stacked image. These unmasked objects can be transient candidates, which are filtered based on their PSF profile and ellipticity parameters to remove false positives (e.g., cosmic rays) and meteors. In the right-hand figure, the schematic diagram illustrates the classification method for unmasked objects (`search_transcand` process). Unmasked objects located in the blue regions are classified as false positives, whereas those appearing as red circles along the stellar sequence are identified as transient candidates.

After passing these selection criteria, human visual inspection of the candidate images is performed. Alt text: A flowchart showing the sequence from data input through processing to transient candidate evaluation.

Table 1. Observed properties of the transient candidate TMG20200322 discovered on March 22, 2020. The UT time listed in the table represents the exposure interval, indicating the start and end times of integration for the detection frames. The 1σ uncertainty of *Gaia* *G*-band magnitude (m_G) and ellipticity is indicated in the brackets. x and y are the position of the flux barycenter and x_{peak} and y_{peak} are the position of the peak pixel. The ellipticity and source position measurements were performed with a threshold of 1σ of the background rms.

Frame No.	UT (exposure interval)	m_G	Ellipticity	x, y (pixel)	$x_{\text{peak}}, y_{\text{peak}}$ (pixel)
108	15:02:24.043 – 15:02:25.043	16.89 (0.11)	0.16 (0.13)	1603.0, 1008.0	1603.0, 1008.0
109	15:02:25.043 – 15:02:26.043	16.65 (0.09)	0.50 (0.05)	1605.5, 1005.2	1603.0, 1007.0

(Chambers et al. 2016) and found no possible optical counterparts within a radius of 5 arcsec. We use the archival Pan-STARRS1 (PS1) stack images in g, r, i, y, z -bands to constrain the magnitude of the optical candidate. We calculate the 5σ limiting magnitude of the PS1 images by putting circular apertures with radius of 5 pixels ($\simeq 1.25''$) at random sky locations. We derive limiting magnitudes of 23.25, 22.45, 22.83, 21.22, 22.26 mag for the g, r, i, y, z bands, respectively. No transient event including GRBs within a radius of 1 arcmin of the TMG20200322 coordinates has been reported on the Transient Name Server (TNS)⁴ before or after the time of its discovery. We searched the following catalogs of multiwavelength survey sources: Two Micron All Sky Survey (2MASS; near-IR), Galaxy Evolution Explorer (GALEX; UV) and Fermi Gamma-ray Space Telescope via NASA's HEASARC archive catalog service⁵, and the Very Large Array/FIRST survey (1.4 GHz Radio)⁶. No

counterpart is found within a 10 arcsec radius of the transient.

5 Discussions

5.1 Near-field effects

We first discuss the possibility that the transient candidate TMG20200322 could be explained by near-field effects: objects subject to temporary local illumination (e.g. aircraft, dust, insects), and optical artifacts such as ghost images or stray light.

For nearby illuminated objects, the Kiso Schmidt telescope (diameter of 105 cm) focused at infinity would produce significantly defocused images. For example, a point source at a distance of 10 km, corresponding to a typical altitude of an aircraft, would be defocused by approximately 20 arcseconds. Objects at closer distances would be even more severely defocused. This is inconsistent with the observed sharp PSF (~ 3 arcsec FWHM), making near-field explanations increasingly implausible. Moreover, an aircraft would be expected to appear bright and move across the im-

⁴ <https://www.wis-tns.org>

⁵ <https://heasarc.gsfc.nasa.gov>

⁶ <http://sundog.stsci.edu/cgi-bin/searchfirst>

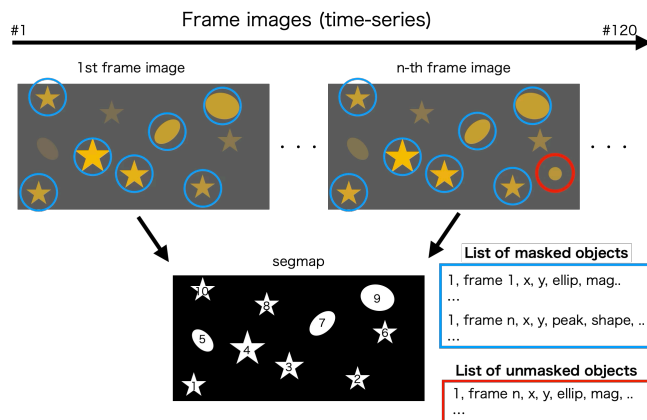


Fig. 4. A schematic picture of how to assign masked/unmasked objects with a segmap. Each object detected in each frame (marked as red and blue circles) is assigned segmap IDs by referring to the segmap. Finally two output catalogs of masked objects and unmasked objects including transient candidates are created. We then search for transients from the unmasked objects. Alt text: Diagram showing how objects detected in time-series frames are compared with a segmentation map and sorted into masked and unmasked object lists.

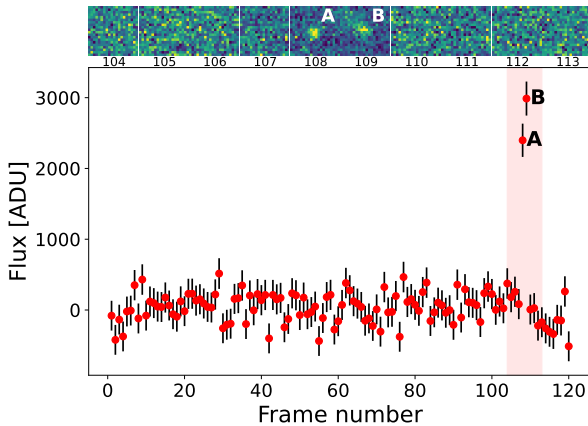


Fig. 5. Forced photometry of the transient candidate TMG20200322. The error bars indicate the 1σ uncertainties calculated from the sum of the Poisson noise and the background errors. We highlight the red-shaded region at the detection frames of TMG20200322 (frame number 108 and 109) labeled as A and B and the corresponding 10 consecutive frame image cutouts (frame number from 104 to 113) are shown in the upper panel. Each cutout has 24 arcsec (20 pixels) on a side, oriented with North up and East to the left. Lower and upper percentiles of 1.0 % and 99.5 % of the pixel values are used to normalize the scale of each cutout. Alt text: Graph showing flux versus frame number, highlighting two peaks labeled A and B. Above the graph, small image cutouts from consecutive frames are displayed.

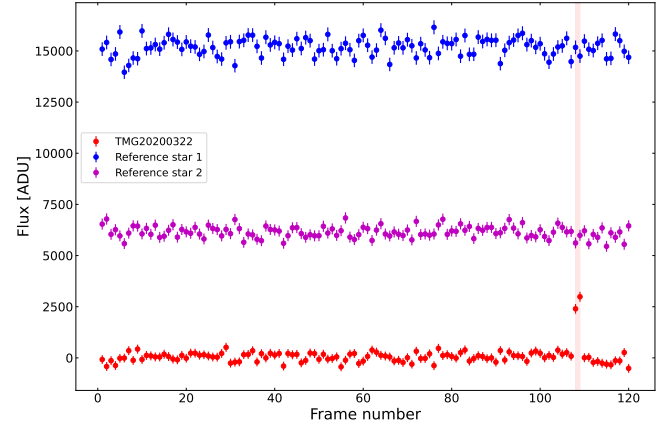


Fig. 6. Comparison of light curves of the two reference stars selected from the *Gaia* DR3 catalog close to the position of TMG20200322. Ref. star 1; $G = 14.96$ mag, $(\text{RA}, \text{Dec})_{\text{J}2000.0} = (12^{\text{h}}18^{\text{m}}32^{\text{s}}.0, -4^{\circ}55'58''.5)$, and Ref. star 2; $G = 15.95$ mag, $(\text{RA}, \text{Dec})_{\text{J}2000.0} = (12^{\text{h}}18^{\text{m}}14^{\text{s}}.0, -4^{\circ}54'34''.9)$. Red vertical shaded region indicates the time of detection of TMG20200322 (108-th and 109-th frames). The error bars denote 1σ photometric uncertainties. Alt text: Light curves of a transient candidate and two reference stars with detection highlighted.

age during the exposure, producing a continuous trail rather than the discrete elongated PSF observed in a single frame.

Regarding optical artifacts such as ghost images or stray light, we note the following: (1) Ghosts do not vary on timescales of a single exposure of 1 s. (2) While stray light from external sources could enter the optical system by chance and form an image, such artifacts generally do not produce images as sharp as observed. We have found no similar artifacts that could be attributed to systematic optical effects. These considerations allow us to confidently rule out near-field effects, ghost images, and stray light as explanations for TMG20200322.

5.2 PSF distortion due to atmospheric fluctuations

Atmospheric fluctuations blur the light from stars, distort the PSF in the image. Megias Homar et al. (2023) investigated how exposure time affects the PSF of very short-duration Fast Optical Bursts (FOBs), which are assumed to be the optical counterparts to FRBs. They simulated observations of the Rubin/LSST to compare spatial brightness distributions of FOBs, assuming a FOB duration of 15 ms. The results showed that FOBs with 15 ms duration exhibit a PSF that is distinctively different from that of steady sources when observed with a LSST's nominal exposure of 15 s. However, the spatial extent of the atmospherically distorted PSF remains confined within the seeing disk.

5.2.1 Comparison with field stars

To verify that the elongated image of TMG20200322 is not due to atmospheric fluctuations, we perform a shape variability comparison with field stars. We select 10 reference stars within the same 120-frame data cube with signal-to-noise ratio (S/N) ranging 10–15 from the *Gaia* DR3 catalog (Gaia Collaboration et al. 2023), ensuring comparable photometric quality to that of TMG20200322 (S/N of ~ 10.2 and ~ 12.4 on the 1st and 2nd frames). To select single stars with good astrometric solutions, we impose the following selection criteria on the *Gaia* sources: `non_single_star` = 0 and `renormalised unit weight error ruwe` < 1.4. We measure semi-

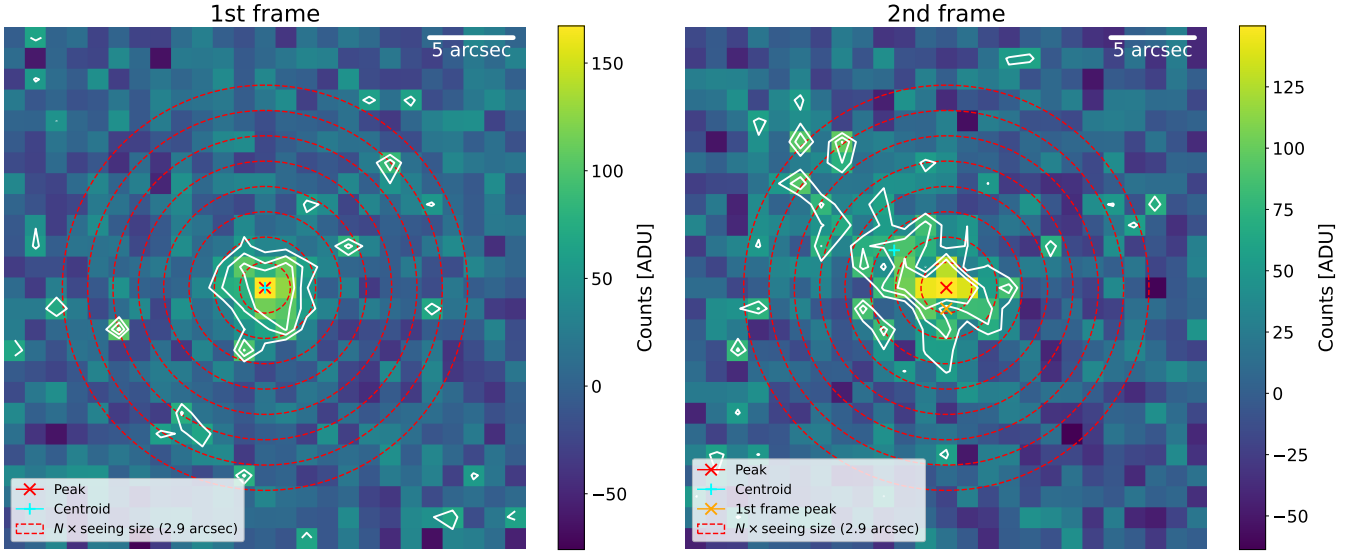


Fig. 7. Zoomed-in images of TMG20200322. The contours with white lines at 2.0, 3.0, and 4.0 σ levels of the background noise are overlaid. Peak (red) and centroid (cyan) pixels are marked in each image (1st frame peak pixel is also marked as orange in the 2nd frame image). The red dashed circles indicate N times the size of seeing FWHM (2.9 arcsec). The cutout image size is $30'' \times 30''$ and the top is north and the left is east.

Alt text: Two zoomed-in frame images with contour lines and overlaid red dashed circles.

major axis and ellipticity for each source using `sep` with a threshold of 1σ of the background rms, in the same manner as was done for TMG20200322. Figure 10 shows the positions of the field stars used in this analysis. It also plots their measured semi-major axes and ellipticities against their S/N. Compared with the field stars, TMG20200322 exhibits significantly larger values for both shape parameters. The mean semi-major axis (a) and ellipticity (e) of the field stars are $\langle a \rangle = 1.85 \pm 0.22$ and $\langle e \rangle = 0.17 \pm 0.10$, respectively. This low ellipticity is consistent with the nearly circular PSF ($e \approx 0$) expected from atmospheric seeing, confirming that the field stars are not systematically elongated. In contrast, TMG20200322 exhibits a semi-major axis of $a \approx 4.3$ and an ellipticity of $e \approx 0.5$. These values correspond to deviations of 11.1σ and 3.2σ from the mean of the reference population, respectively. These results demonstrate that the elongation of TMG20200322 is not caused by atmospheric or systematic instrumental effects, but is instead of intrinsic origin.

5.2.2 Constraints from high-speed observations

To place constraints on the timescale of the flash duration of TMG20200322, we perform additional high-speed observations of the Pleiades open cluster at 57 fps (17.4 ms exposure time) using the partial readout mode of Tomo-e Gozen. While these data were taken under different observing conditions (mean seeing size of 4.0 ± 0.3 arcsec) than the TMG20200322 detection, they provide useful constraints on atmospheric effects on the event timescale (e.g., Megias Homar et al. 2023). We use stars with S/N of $10 \sim 15$ as in the previous analysis.

We find that TMG20200322 exhibits a significantly higher semi-major axis and ellipticity than stars observed at 57 fps, with deviations of 15.5σ and 6.1σ , respectively. Although the atmospheric conditions for this comparison are not identical, the degree of elongation observed in TMG20200322 is unlikely to be replicated in images of stars taken with ~ 20 ms exposure time. Therefore, despite the limitations, this analysis strongly suggests that extreme atmospheric seeing alone cannot account for the elongation of TMG20200322.

gation of TMG20200322.

5.3 Potential astrophysical origins

Here we discuss the potential astrophysical origins of TMG20200322 based on its observed properties and compare the corresponding event rates. We consider two scenarios for the source: (a) impact flash caused by a collision between two celestial bodies, and (b) a terrestrial atmospheric phenomenon, specifically a head-on meteor. Although it is difficult to explain the elongated component of the TMG20200322 image by atmospheric fluctuations alone, we also consider possible origins of TMG20200322 under the assumption that the PSF is not elongated in the Appendix.

5.3.1 Meteoroid Impact Flash on Near-Earth Asteroid Surfaces

To account for the elongated component of the TMG20200322 image and its brief duration ($\lesssim 2$ s), we consider an impact flash produced by the collision of two celestial bodies. When a centimeter-sized meteoroid impacts the Moon at velocities of several tens of kilometers per second, part of its kinetic energy is converted into luminous energy, and ground-based telescopes typically observe a flash of magnitude $5 \sim 10$ in visible to near-infrared light (Bellot Rubio et al. 1998; Ortiz et al. 2000). This phenomenon, known as a lunar impact flash, typically lasts less than 1.0 s (e.g., Suggs et al. 2014; Liakos et al. 2024). By replacing the Moon with a Near-Earth Asteroid (NEA), we estimate the detection rate of meteoroid impact flashes on NEA surfaces.

Although the distance to TMG20200322 is unknown, we estimate an upper limit to the event's distance based on the elongation of the image. The extended component from the core of the PSF ($2 \times \text{FWHM} \sim 5.8$ arcsec) is approximately 10 arcsec (see Figure 7). Due to the temporal resolution of our observations is one second, the actual duration of TMG20200322 may be shorter than the exposure time. We assume that the apparent image elongation is produced by ejecta moving an angular distance of 10 arcsec

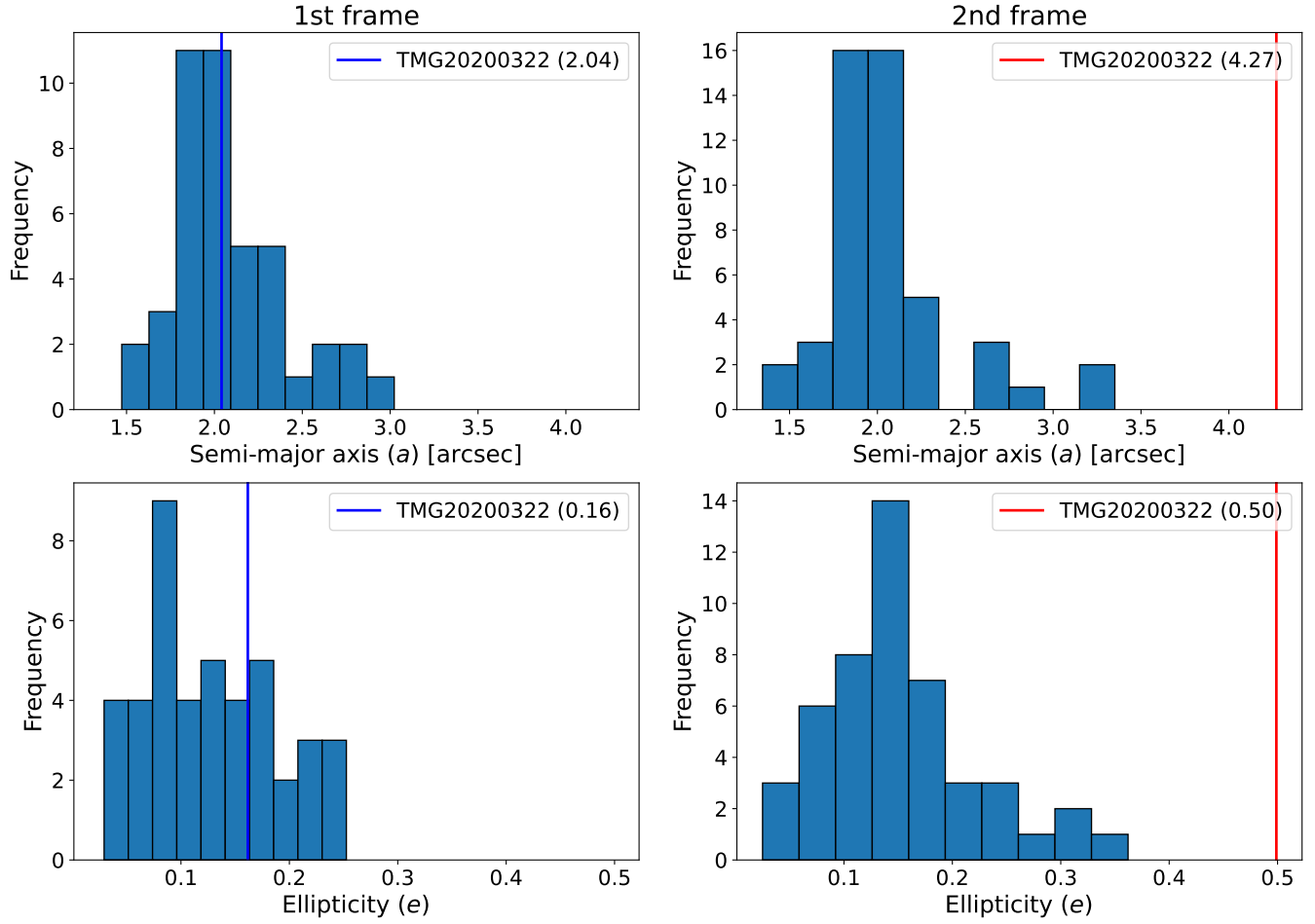


Fig. 8. Distribution of shape parameters for field stars compared with TMG20200322. Top panels: semi-major axis (a) in arcseconds; bottom panels: ellipticity (e). Left and right panels correspond to the 1st and 2nd detection frames, respectively. Vertical lines show the measured values for TMG20200322 (blue: 1st frame; red: 2nd frame), as indicated in the brackets in the figure legends. Field stars have S/N ratios between 10 and 15. All shape parameters are measured at an isophotal level of 1σ above the background noise. Alt text: Four histogram panels arranged in a 2-by-2 grid.

over a period of one second. We use the typical collision velocity between NEAs (Bottke & Greenberg 1993) of 15 km s^{-1} to calculate the length that the ejecta moves in one second. The ejecta velocity caused by a collision event is known to be in the range of $v_{\text{ej}} \sim 10^{-4} - 10^{-1} v_{\text{col}}$, where v_{col} is the collision velocity (Ferrari et al. 2022). Since the elongation on the image is the projection component of the ejecta on the celestial plane, we can estimate the ejecta length $l_{\text{ej}} = v_{\text{ej}} \cos \theta \cdot t$, where θ is the projection angle. Substituting maximum ejection velocity of $v_{\text{ej}} = 1.5 \text{ km s}^{-1}$, $\theta = 0 \text{ deg}$, and $t = 1.0 \text{ s}$, we get the maximum length of $l_{\text{ej}} \sim 1.5 \text{ km}$. With the observed angular distance of the ejecta ($\sim 10 \text{ arcsec}$), we can calculate the distance to the event by $d \sim 20,626 \times l$. Consequently, d can be constrained to be $d \lesssim 3.1 \times 10^4 \text{ km}$.

The NELIOTA project (Xilouris et al. 2018; Liakos et al. 2024) conducted simultaneous dual-band (R and I) monitoring of the lunar surface to detect hundreds of lunar impact flashes. Observations covered ~ 276 hours until June 22, 2023, with a camera field of view (FoV) of $17'.0 \times 14'.4$. We fit the NELIOTA cumulative R -band magnitude distribution using an exponential form, where a and r are the fitting parameters:

$$N(\leq m) = a \times r^m \quad (1)$$

The best-fit parameters are $a = 0.0023 \pm 0.0016$ and $r = 2.98 \pm$

0.21 (Figure 11). Here, $N(\leq m)$ represents the total number of impact flash events detected throughout the NELIOTA observation campaign. The total observed lunar surface area and observation time are $A_{\text{obs}} = 3.1 \times 10^6 \text{ km}^2$ and $T_{\text{obs}} = 276 \text{ h}$ ($9.9 \times 10^5 \text{ s}$), respectively. We define the impact frequency density, Φ_{moon} , by normalizing the cumulative count by these parameters:

$$\Phi_{\text{moon}}(\leq m) = \frac{N(\leq m)}{A_{\text{obs}} \times T_{\text{obs}}} = \frac{0.0023 \times 2.98^m}{3.1 \times 10^6 \times 9.9 \times 10^5} \text{ [events km}^{-2} \text{ s}^{-1}\text{]} \quad (2)$$

For the detected magnitude $m \approx 16.8$:

$$\Phi_{\text{moon}}(\leq 16.8) \sim 6.9 \times 10^{-8} \text{ [events km}^{-2} \text{ s}^{-1}\text{]} \quad (3)$$

We define the impact frequency at a distance d by scaling the known lunar impact rate. Since the apparent magnitude varies with distance, we correct the magnitude threshold by the distance modulus (scaling by $5 \log_{10}(d/d_{\text{moon}})$). This corrected magnitude is then substituted into the lunar cumulative distribution function to obtain the expected frequency density at the target distance. For simplicity, we assume that the meteoroid flux measured on the lunar surface applies uniformly to NEA surfaces, and we ignore variations due to gravitational focusing or heliocentric orbital clustering. This assumption makes our estimate conservative and sufficient for an order-of-magnitude constraint.

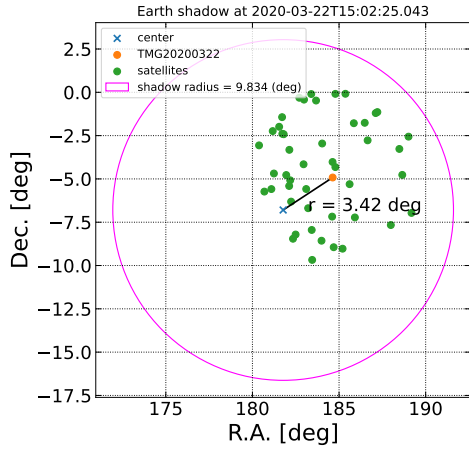


Fig. 9. The coordinates of TMG20200322 and the Earth's shadow region at GEO. The blue cross indicates the center of the Earth's shadow at the time of discovery of TMG20200322, and the shadow region is represented by the magenta circle. TMG20200322, marked as an orange point, is located inside the shadow, approximately 3.42 deg away from the shadow center. The green points represent artificial bodies found within a 5-degree radius from the coordinate of TMG20200322 by the Space Track database. Alt text: Scatter plot in equatorial coordinates showing an orange point inside a magenta circle, with a blue cross marking the center and multiple green points scattered around.

Table 2. Scaled impact frequency density for 16.8 mag impact flash case with various distances

Distance [km]	$\Phi(d, \leq 16.8)$ [events $\text{km}^{-2} \text{s}^{-1}$]
500	4.8×10^{-1}
5,000	2.0×10^{-3}
10,000	4.0×10^{-4}
31,000	2.7×10^{-5}

$$\Phi(d, \leq m) = \Phi_{\text{moon}} \left(\leq m - 5 \log_{10} \frac{d}{d_{\text{moon}}} \right) \text{ [events } \text{km}^{-2} \text{s}^{-1}] \quad (4)$$

Table 2 shows the scaled impact frequency densities for different distances. We adopt the NEA population model from Harris & Chodas (2021) to estimate the number of NEAs; $N(D) \sim 2 \times 10^2$, $\sim 1 \times 10^4$, and $\sim 1 \times 10^7$ objects with diameters $D = 1.0$, 0.1 , and 0.01 km, respectively. Assuming a uniform spatial distribution within a volume of $V \sim 1 \text{ AU}^3$ ($\sim 3 \times 10^{24} \text{ km}^3$), each size bin yields a number density $n(D) = N(D)/V$. This assumption likely underestimates the local NEA number density near Earth, and thus makes our detection probability estimate conservative. For a given NEA size and distance, the expected number of targets crossing the FoV of Tomo-e Gozen during observations is:

$$N_{\text{transit}}(D, d) = n(D) V_{\text{survey}}(d), \quad (5)$$

where the survey volume swept by the FoV of Tomo-e Gozen is

$$V_{\text{survey}}(d) = w_{\text{FoV}}^2(d) V_{\text{rel}} T_{\text{obs}}, \quad (6)$$

where $w_{\text{FoV}}(d)$ is the linear width of the FoV at distance d , V_{rel} is a representative sky-plane relative velocity of NEAs (we adopt 15 km s^{-1}), and $T_{\text{obs}} = 44 \text{ h}$ is our total observation time. We adopt a square FoV equivalent to the total area of 17.8 deg^2 . The expected number of flashes brighter than m_{lim} that occur on the surface of each transiting NEA is

$$N_{\text{flash}}(D, d) = \Phi(d, \leq m_{\text{lim}}) A_{\text{NEA}}(D) t_{\text{transit}}(d), \quad (7)$$

where $A_{\text{NEA}} = \pi D^2$ is the physical surface area of NEA and $t_{\text{transit}}(d) = w_{\text{FoV}}(d)/V_{\text{rel}}$ is the transit timescale. The total number of detectable flashes expected during the observation is then

$$N_{\text{expected}}(D, d) = N_{\text{transit}}(D, d) N_{\text{flash}}(D, d). \quad (8)$$

We compute $N_{\text{expected}}(D, d)$ across the parameter space (D, d) and present the results in Table 3. Under the assumptions adopted, no combination of parameters satisfies $N_{\text{expected}} \geq 1$, indicating that the probability of detecting a meteoroid impact flash on an NEA with Tomo-e Gozen during 44-hour observations is extremely small. Therefore, a NEA-meteoroid collision flash scenario of this nature cannot plausibly explain the detection of TMG20200322.

Table 3. Order-of-magnitude estimates of expected detectable flashes for our Tomo-e Gozen observation (44 h, 17.8 deg^2).

D [km]	500 km	5,000 km	10,000 km	31,000 km
0.01	4×10^{-12}	2×10^{-11}	2×10^{-11}	5×10^{-11}
0.1	4×10^{-13}	2×10^{-12}	2×10^{-12}	5×10^{-12}
1.0	7×10^{-13}	3×10^{-12}	5×10^{-12}	9×10^{-12}

5.3.2 Head-on meteors

As a potential terrestrial atmospheric origin of TMG20200322, we assume a head-on meteor. This scenario involves a meteor traveling directly towards the telescope along its line of sight, causing it to be detected as a stationary point source. Given that the coordinates and discovery time of TMG20200322 are not associated with any meteor shower, we consider meteors of sporadic origin. The typical duration of meteor luminescence ranges from ~ 0.1 – 1.2 s, and the fraction of sporadic meteors with durations of > 0.8 s is estimated to be $\sim 8\%$ (Betzler & de Sousa 2022). We estimate the probability of a head-on meteor with different durations of $\tau = 1.0$ s and 0.1 s, since the exposure time of our Tomo-e Gozen observations (1.0 s) may be longer than the duration of meteors. In the case of a duration of 0.1 s, the peak brightness needs to be corrected for the dilution effect observed in a longer exposure time. The peak magnitude m_P is expressed as

$$m_P = -2.5 \log_{10} \left(\frac{T_{\text{exp}} 10^{-0.4m_0}}{\tau} \right), \quad (9)$$

where τ is the duration of an object and m_0 is the magnitude observed with an exposure time of T_{exp} . For the observed magnitude of TMG20200322, $m_0 = 16.8$ mag (the average of two frames), the corresponding peak magnitude is $m_P = 14.3$ mag for $\tau = 0.1$ s and $T_{\text{exp}} = 1.0$ s.

Here we assume that meteors occur at a constant altitude of $h = 100$ km and observations are conducted at an averaged zenith angle of $\theta = 45$ deg. The effective FoV of Tomo-e Gozen (17.8 deg^2) corresponds to a solid angle $\Omega_{\text{FoV}} \approx 5.4 \times 10^{-3}$ sr. The line of sight at zenith angle θ intersects the horizontal plane at altitude h along a slant distance $D = h/\cos \theta$. The area on a spherical surface at distance D is $A_{\text{sphere}} = \Omega_{\text{FoV}} D^2$. Projecting this onto the horizontal plane, accounting for the oblique viewing angle, gives:

$$A = \frac{\Omega_{\text{FoV}} D^2}{\cos \theta} = \frac{\Omega_{\text{FoV}} h^2}{\cos^3 \theta}. \quad (10)$$

For our parameters ($h = 100$ km, $\theta = 45$ deg), this yields $A \approx 1.5 \times 10^2 \text{ km}^2$.

We use the cumulative number flux of sporadic meteors in the

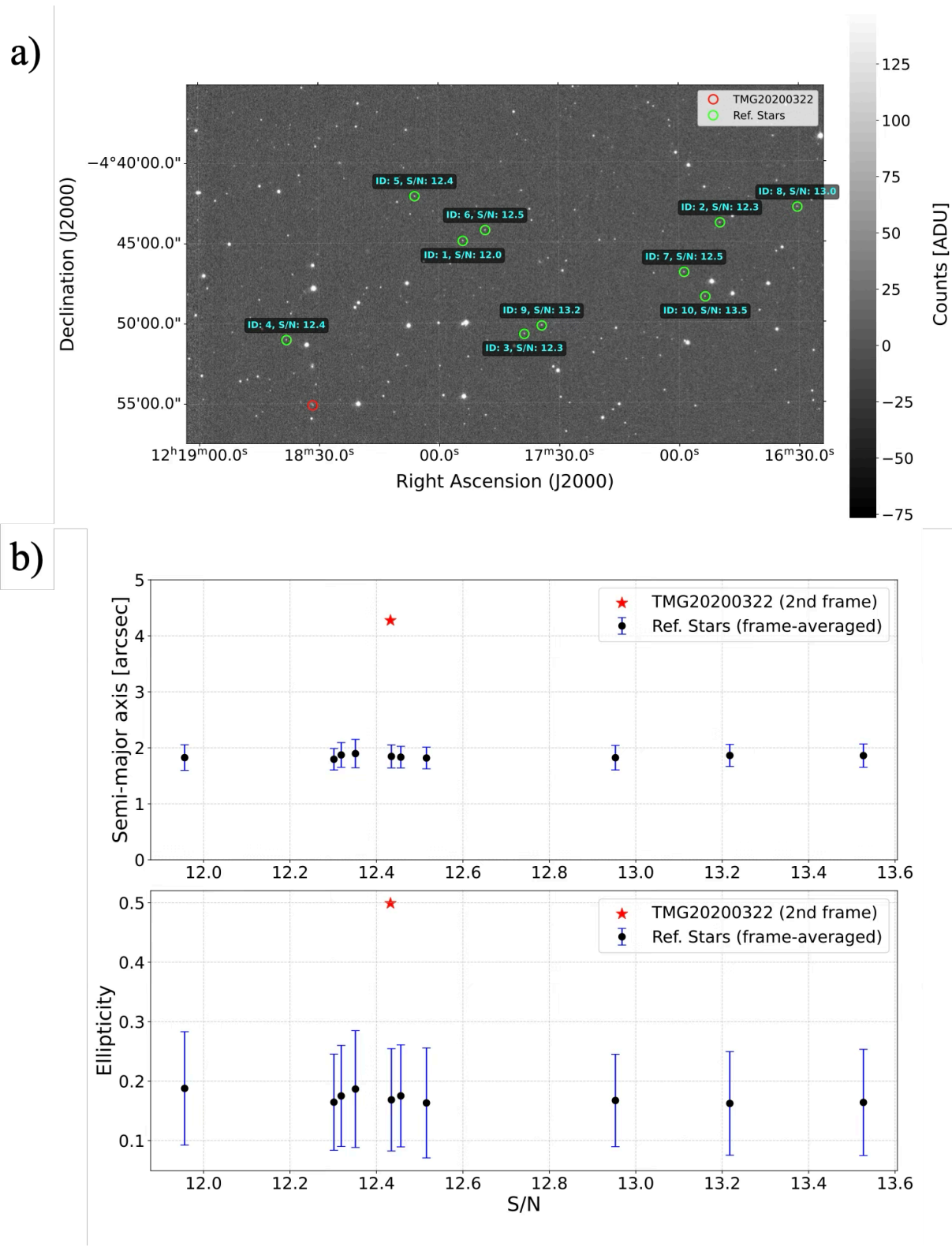


Fig. 10. Shape variability of the field stars in the detection data cube of TMG20200322. (a) Frame image (2nd detection frame of TMG20200322) showing the positions of the 10 field stars, labeled with their source IDs, S/N values, and the number of detected frames. (b) Semi-major axis and ellipticity of the field stars as a function of S/N, with the values for TMG20200322 indicated by red stars. Error bars for each plot indicate 1σ uncertainty in both measurements. Alt text: Two-panel figure: the left panel shows field star positions marked on the image, while the right panel presents two measurement plots, with TMG20200322 highlighted as red star.

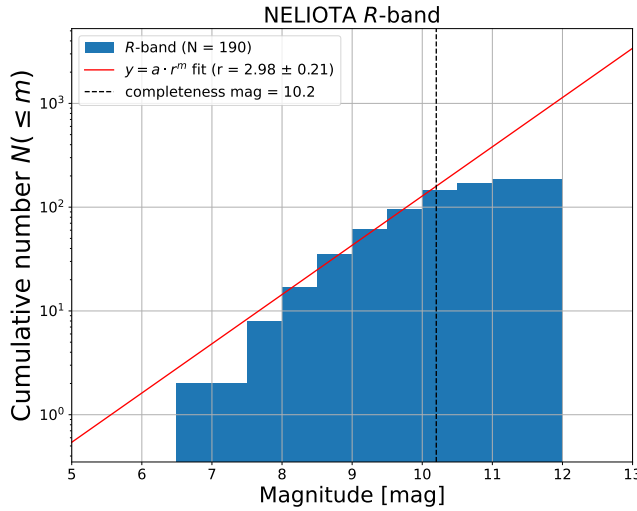


Fig. 11. Cumulative number distribution of the lunar impact flashes observed by NELIOTA project until June 22th, 2023. The black dashed vertical line indicates the completeness magnitude used for the fitting. Alt text: Histogram of cumulative number versus magnitude with fit and reference line.

V -band from Ohsawa et al. (2020), fitted by an exponential form as a function of magnitude:

$$F \approx 1 \times 10^{-5} \times 3.52^{M_V} \text{ h}^{-1} \text{ km}^{-2}, \quad (11)$$

where M_V is the absolute magnitude observed at a distance of 100 km. We then extrapolate the relation to the fainter side to obtain the meteor flux by approximating the V -band and the *Gaia G*-band as equivalent.

For our observation geometry with a zenith angle of 45 deg, the effective distance to the meteor layer is $D = 100/\cos(45 \text{ deg}) \approx 141.4$ km. Under the approximation that the V -band and Gaia G -band are equivalent, we obtain absolute magnitudes of $M_V(\tau = 1.0 \text{ s}) \approx 16.0$ mag and $M_V(\tau = 0.1 \text{ s}) \approx 13.5$ mag for the two timescale scenarios. Extrapolating Equation 11 to these faint magnitudes and accounting for the fact that only $\sim 8\%$ of meteors persist longer than 0.8 s (Betzler & de Sousa 2022), we calculate:

$$F(\tau = 1.0 \text{ s}) \sim 4 \times 10^2 \text{ h}^{-1} \text{ km}^{-2} \quad (12)$$

$$F(\tau = 0.1 \text{ s}) \sim 2 \times 10^2 \text{ h}^{-1} \text{ km}^{-2}. \quad (13)$$

The expected number of meteors detected in our observation N can then be estimated as the product of meteor flux, projected area at the meteor layer, and the total observation time $N = F \cdot A \cdot t_{\text{obs}}$.

$$N(\tau = 1.0 \text{ s}) \sim 3 \times 10^6 \quad (14)$$

$$N(\tau = 0.1 \text{ s}) \sim 2 \times 10^6 \quad (15)$$

For a meteor to appear as a stationary source in our sidereal tracking observations, it must move in such a way that its apparent motion cancels the telescope tracking ($15''/\text{s}$ in the RA direction). The geometric probability is given by the ratio of solid angles:

$$p_{\text{geom}} = \frac{\Omega_{\text{PSF}}}{\Omega_{\text{meteor}}} = \frac{\pi(\text{FWHM}/2)^2}{2\pi(1 - \cos\theta_{\text{eff}})}, \quad (16)$$

where $\text{FWHM} = 3.0''$ is the seeing disk size, and θ_{eff} is the effective zenith angle for meteor incidence. We adopt $\theta_{\text{eff}} = 60$ deg as a representative value, considering that meteors can arrive from a range of zenith angles. This yields:

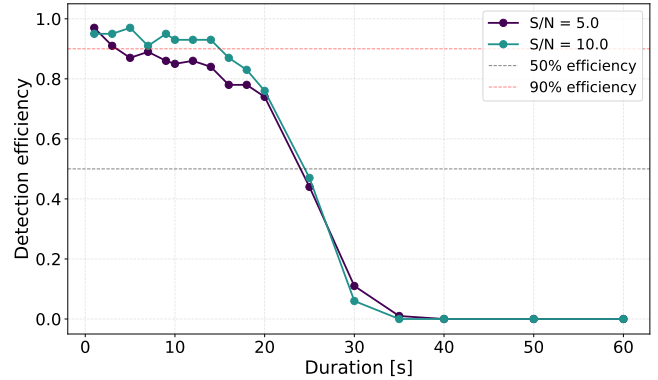


Fig. 12. Detection efficiency as a function of transient duration for artificial transients with $\text{S/N} = 5.0$ and 10.0 . The horizontal dashed lines indicate 50% (gray) and 90% (red) efficiency, respectively. Alt text: A line graph showing two curves with two reference percentage levels.

$$p_{\text{geom}} = \frac{\pi \times (1.5'')^2 \times (\pi/648000)^2}{2\pi(1 - \cos 60^\circ)} \approx 5.3 \times 10^{-11}. \quad (17)$$

The expected number of head-on meteors detected in our survey E is given by $N \times p$,

$$E(\tau = 1.0 \text{ s}) = N(\tau = 1.0 \text{ s}) \times p_{\text{geom}} \approx 2 \times 10^{-4} \quad (18)$$

$$E(\tau = 0.1 \text{ s}) = N(\tau = 0.1 \text{ s}) \times p_{\text{geom}} \approx 1 \times 10^{-4}. \quad (19)$$

In both cases, the expected number of events is four orders of magnitude smaller than unity. In addition, such faint meteors ($M \gtrsim 14.3$ mag) have not been detected in Tomo-e Gozen 2 fps observations (Ohsawa et al. 2020). Extremely faint meteors are unlikely to exhibit luminescence lasting $\sim 0.1\text{--}1.0$ s because of their low kinetic energy. Therefore, it remains unlikely that TMG20200322 originates from meteors.

5.4 Event rate of second-timescale transients

We discuss the event rate of second-timescale transients from the single detection of TMG20200322. We calculate the event rate of transients, R_{trans} , in units of per square degree per day ($\text{deg}^{-2} \text{ day}^{-1}$), as

$$R_{\text{trans}} = \frac{N_{\text{trans}}}{\epsilon E_A}, \quad (20)$$

where N_{trans} is the number of detected transients, and ϵ is the detection efficiency. We perform injection-recovery tests using simulated transients (2D Gaussians) on real Tomo-e Gozen data cubes with varying durations. For each combination of S/N (5.0 and 10.0) and duration, we inject 100 synthetic transients at random spatial positions and calculate the detection efficiency as the fraction of successfully recovered events. In Figure 12, we find that our pipeline can reliably detect transients lasting from 1 s and up to ~ 20 s. The measured detection efficiency is $\geq 90\%$ for transients with $\text{S/N} = 10$ (similar S/N to that of TMG20200322) lasting 1–15 s. We adopt $\epsilon = 0.90$ and consider target transients with durations of 1–15 s in the following calculations. E_A is the effective areal exposure, defined as the product of effective field of view explored and the total monitored exposure time:

$$E_A = \text{FoV}_{\text{eff}} \times t_{\text{eff}}. \quad (21)$$

From the limiting magnitude distribution shown in Figure 2, we calculate t_{eff} by excluding data with limiting magnitudes shallower than $m_{\text{lim}} = 16$ mag, resulting in $t_{\text{eff}} \sim 44.4$ hours (~ 1.85

days). In our transient detection pipeline, the objects detected in the stacked images are masked, which reduces FoV_{eff} for the transient search. We calculate the fraction of pixels occupied by masked objects to be an average of 4.5% of the image of 2000×1128 pixels. Furthermore, we exclude 10 pixels from the edges along both the x - and y -axes of the image for object detection, corresponding to approximately 3% of the image area, resulting $\text{FoV}_{\text{eff}} = 17.78 \text{ deg}^2$.

The upper and lower limits for a single event ($N_{\text{trans}} = 1$) at the 95% confidence level are $n_{\text{upper}} = 4.744$ and $n_{\text{lower}} = 5.13 \times 10^{-2}$ events, respectively, based on Poisson statistics (Gehrels 1986). We take these uncertainties into account for the event rate calculation and derive

$$R_{\text{trans}} = (3.4 \times 10^{-2})^{+0.13}_{-0.028} \text{ deg}^{-2} \text{ day}^{-1}. \quad (22)$$

The all-sky rate of FRB population is estimated to be ~ 820 per day above a fluence of 5 Jy ms at 600 MHz (CHIME/FRB Collaboration et al. 2021). Interestingly, the all-sky rate derived from our single detection of TMG20200322 is $\sim 1,400$ per day, which is of the same order as that of the FRB population. Although the PSF elongation makes an extragalactic origin of TMG20200322 unlikely, our result suggests the possible existence of a new population of FRB-like ubiquitous optical transients.

As discussed in the previous section, the plausible astrophysical origin of TMG20200322 remains unclear. Therefore, we also estimate an upper limit on the event rate under the non-detection assumption. We follow the same procedures as described in Richmond et al. (2020) to derive an upper limit with the 95% confidence level. Our upper limit on the event rate of transients with durations ranging from one second to less or equal to 15 seconds ($1 \text{ s} \leq \tau \lesssim 15 \text{ s}$) is estimated to be

$$R_{\text{trans}} \lesssim 0.10 \text{ deg}^{-2} \text{ day}^{-1}. \quad (23)$$

Figure 13 presents our derived event rates for both the single-detection and non-detection cases, compared with values reported in previous and future transient searches targeting short timescales (< 1 hour). In the non-detection case, our derived upper limit constrains ~ 14 times tighter than that of Richmond et al. (2020). The Pi of the Sky project obtained upper limit of an order of 10^3 tighter than our value, but with about 6.5 mag shallower depth than Tomo-e Gozen. Survey depth is a critical factor when discussing the volumetric rate of a given class of transient sources. One of the upcoming high cadence surveys, Argus Array will provide powerful constraints on sub-second and short-duration transients with its unprecedented combination of cadence (down to 0.25 s with ~ 15 mag depth) and sky coverage ($\sim 8,000 \text{ deg}^2$; Law et al. 2022). Such surveys will be crucial for characterizing the population of transients like TMG20200322 and understanding their nature. Although the distance to TMG20200322 is not constrained, surveys with shallow depth are not suitable for exploring the transient sky, particularly for sources of Galactic or extragalactic origin. Our possible discovery of TMG20200322 highlights that searches for second-timescale transients are highly desirable to reveal new populations of optical transients.

6 Summary

In this paper, we present a dedicated 1 fps video monitoring survey of the Earth's shadow region to probe the largely unexplored second-timescale transient sky. Using video frames with a total areal exposure of $\sim 790 \text{ deg}^2 \text{ hour}$, we search for objects with apparent durations of $1 \leq \tau \lesssim 15 \text{ s}$ through our custom detection

pipeline. After human visual inspection, we discover one transient candidate TMG20200322 with a duration of $\lesssim 2 \text{ s}$.

We find that TMG20200322 exhibits an elongated PSF in the second frame, with ellipticity (~ 0.50) and semi-major axis significantly different from field stars. To test whether atmospheric seeing could produce such elongation, we perform additional observations at 57 fps (17.4 ms exposure). Despite poorer seeing conditions in these data ($4.0 \pm 0.3 \text{ arcsec}$), TMG20200322's elongation exceeds that of 57 fps stars by 15.5σ (semi-major axis) and 6.1σ (ellipticity), demonstrating that atmospheric turbulence alone cannot explain the observed PSF morphology. This is consistent with simulations showing that ~ 15 ms flashes remain within the seeing disk (Megias Homar et al. 2023).

We investigate the origins of such second-timescale transients that exhibit an elongated PSF. The expected number of events, such as impact flashes from collisions between near-Earth asteroids (NEAs) and meteoroids in the Earth's vicinity, or head-on meteors, is much less than unity and therefore cannot account for the observed occurrence rate. The derived event rate of both the single-detection and non-detection cases are compared with previous short-duration transient searches. The all-sky rate derived from the single-detection is comparable to that of FRB population, although the physical connection is need to be investigated. Even in the upper limit from the non-detection case, our constraint on the second-timescale transients is ~ 14 times tighter than that of initial work using the prototype model of Tomo-e Gozen. Not only wider and short exposure time but moderate limiting magnitude of ~ 17.5 mag, our present search can capture the transient phenomena which may be missed by shallow-depth surveys such as Pi of the Sky project (Sokołowski et al. 2010).

We have entered an era that requires optical instruments with not only wide FoV and enhanced sensitivity but also high temporal resolution. These capabilities are crucial both for unveiling the nature of known-unknown transients, such as FRBs, and for discovering new astrophysical transients in the universe. Statistical samples of TMG20200322-like events are necessary to confirm their nature. We demonstrate that video observations using the wide-field CMOS camera targeted at the Earth's shadow region can search for transients that may have been overlooked by previous optical surveys. The upcoming operations of Rubin/LSST, with its 8.4 m diameter, will specialize in wide and deep observations (Ivezic et al. 2019). Using the wide-field, high-speed capability of Tomo-e Gozen, we can complement Rubin/LSST by exploring the transient sky on timescales of a few seconds or less.

Acknowledgments

The authors thank the anonymous referee for his/her helpful comments that improved the manuscript. The authors also thank Dr. Tomoki Morokuma and Dr. Kazumi Kashiyama for their valuable suggestions.

Funding

This research was supported by JSPS KAKENHI Grant Numbers JP18H01261, JP18H05223, JP21H04491, JP23K03469, JP24K17081.

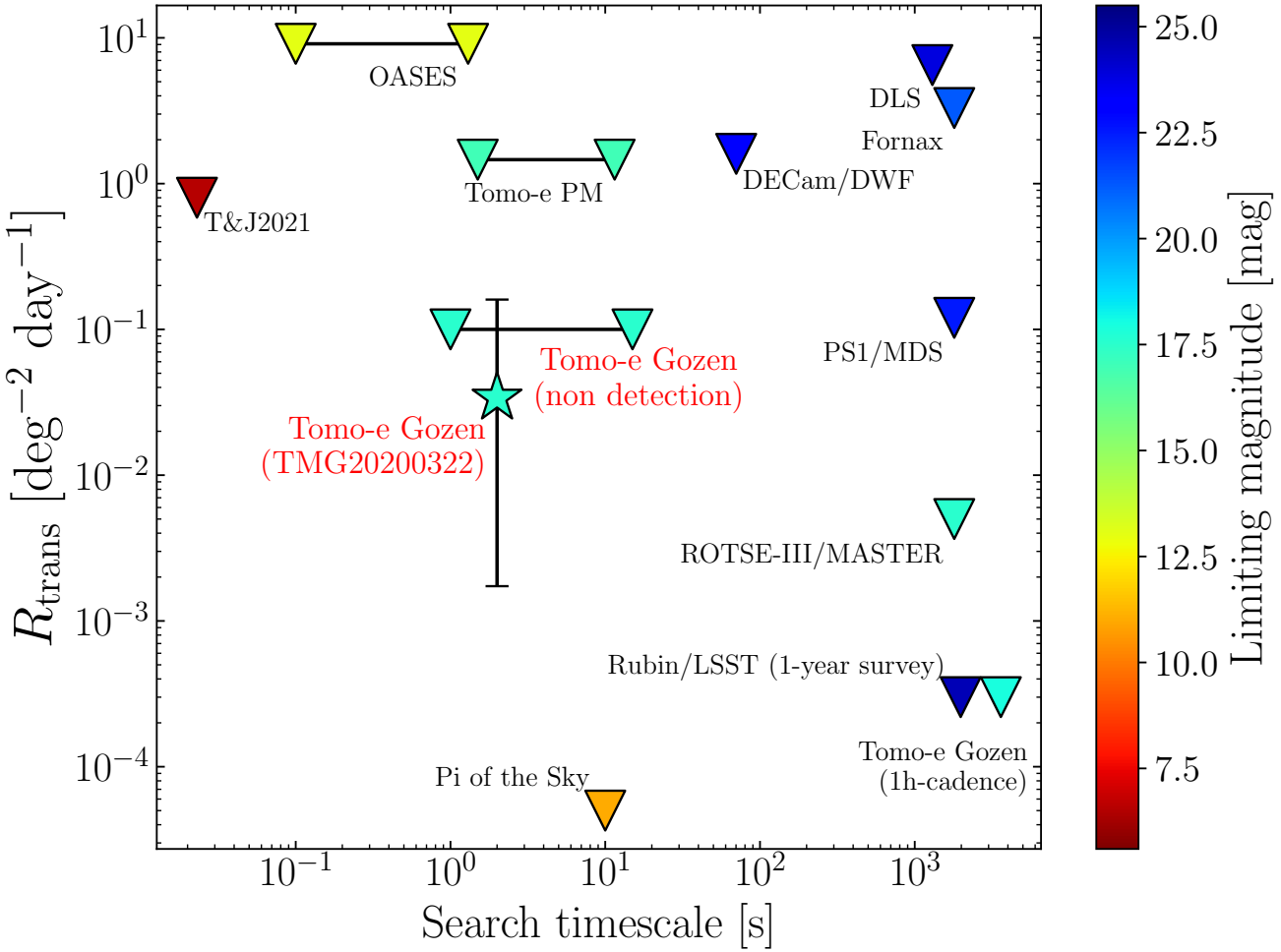


Fig. 13. Event rates of optical transients as a function of search timescale, compiled from short-duration (< 1 hour) transient searches in the literature. The color bar shows the limiting magnitudes of each transient searches. Our derived event rate for TMG20200322 and the upper limit for transients with $1.0 \text{ s} \leq \tau \lesssim 15 \text{ s}$ (non detection case) are indicated in red. Upper limits of the event rates ($\text{deg}^{-2} \text{ day}^{-1}$) by the Tomo-e Gozen high-cadence (1h) survey (Oshikiri et al. 2024), the Deep Lens Survey (DLS; Becker et al. 2004), the Robotic Optical Transient Search Experiment-III (ROTSE-III; Rykoff et al. 2005), the MASTER telescope system (Lipunov et al. 2007), the “Pi of the Sky” project (Sokolowski et al. 2010), the Fornax galaxy cluster survey (Rau et al. 2008), the Pan-STARRS1 Medium-Deep Survey (PS1/MDS; Berger et al. 2013), the Dark Energy Camera Deeper, Faster programme (DECam/DWF; Andreoni et al. 2020), the prototype model of the Tomo-e Gozen camera (Tomo-e PM; Richmond et al. 2020), the Organized Autotelescopes for Serendipitous Event Survey (OASES; Arimatsu et al. 2021) and Tingay & Joubert 2021 (T&J2021) are plotted with their search timescales. The expected upper limit based on one-year operation of the Rubin/LSST main survey (g+r-band combination, 33-min cadence) (Ivezic et al. 2019) is also plotted (the value is derived from Berger et al. 2013). Alt text: Plot of event rate versus search timescale with survey markers. Inverted triangles show upper limits.

Appendix. Galactic and extragalactic origins

The elongation of the PSF in the second frame makes TMG20200322 unlikely that this object is a Galactic or extragalactic source, but we explore possible origins, assuming that the elongation is due to extreme atmospheric turbulence.

As a potential source of Galactic origin, we consider a short-duration stellar flare. Given that TMG20200322 lacks an optical counterpart in the PS1 source catalog with a depth of ~ 23 mag in the r_{PS1} -band, its nature would be intriguing. If this is a stellar flare, the required brightening rate would exceed ~ 6 mag per second, equivalent to a flux increase of about 250 times. Qualitatively, the duration of stellar superflares correlates with flare energy, meaning that shorter-duration flares typically exhibit lower magnification rates (Maehara et al. 2015). Aizawa et al. (2022) searched for short-duration stellar flares from a one-second-cadence M-dwarf survey by Tomo-e Gozen and detected 22 flares with rise times (the time from the beginning of the stellar flare to its peak) of $5 \text{ s} \lesssim t_{\text{rise}} \lesssim 100 \text{ s}$ and flare amplitudes of $\approx 0.5 - 20$ times the quiescent luminosity. Given the relation between the rise time and amplitude of stellar flares (Aizawa et al. 2022), an increase in flux by a factor of more than 250 in one second is not expected unless an extreme case is considered.

As a transient of extragalactic origin, here we assume that TMG20200322 is an optical counterpart to FRBs. Although simultaneous observations using radio and optical bands (Hardy et al. 2017; Niino et al. 2022; Hiramatsu et al. 2023), and follow-up observations by multiple wavelengths have been conducted within hours of a burst (Petroff et al. 2015; Tominaga et al. 2018), there has been no detection of optical emission from any FRB. Interestingly, a model involving a magnetar giant flare producing an FRB predicts an optical flash with duration of ~ 0.1 to ~ 1 s (Beloborodov 2020). The luminosity is expected to be $L_{\text{iso, peak}} \sim 10^{44-45} \text{ erg/s}$, occurring synchronously with an FRB (Beloborodov 2020). We follow the same technique by Chen et al. (2020) to calculate the fluence ratio of the optical and radio bands of FRBs using a cumulative fluence distribution derived from independent radio observations.

$$\eta(\nu_c) \equiv \frac{F_{\text{optical}}}{F_{\text{radio}}} = \frac{\nu_{1, \text{optical}} \cdot F_{\nu, \text{optical}}}{\nu_{1, \text{radio}} \cdot F_{\nu, \text{radio}}}, \quad (\text{A1})$$

where the central frequency ν_c for Tomo-e Gozen is $\nu_c = 6.0 \times 10^{14} \text{ Hz}$ ($\lambda_c = 500 \text{ nm}$). F_{optical} and F_{radio} are the band-integrated fluences, $F_{\nu, \text{optical}}$ and $F_{\nu, \text{radio}}$ are specific fluences, and $\nu_{1, \text{optical}}$ and $\nu_{1, \text{radio}}$ are the lower frequency bounds for optical and radio bands, respectively. This method allows us to test whether our assumption of TMG20200322 to be an optical counterpart to FRBs is valid or inconsistent. Although the origin of TMG20200322 remains unidentified, the derived $\eta(\nu_c)$ is consistent with the theoretical model for FRBs which involves a magnetar giant flare (Beloborodov 2020) (Figure 14).

References

Aizawa, M., Kawana, K., Kashiyama, K., et al. 2022, PASJ, 74, 1069,
 Andreoni, I., Cooke, J., Webb, S., et al. 2020, MNRAS, 491, 5852,
 Arcavi, I., Wolf, W. M., Howell, D. A., et al. 2016, ApJ, 819, 35,
 Arimatsu, K., Tsumura, K., Usui, F., Ootsubo, T., & Watanabe, J.-i. 2021,
 AJ, 161, 135,
 Barbary, K. 2016, The Journal of Open Source Software, 1, 58,
 Becker, A. C., Wittman, D. M., Boeshaar, P. C., et al. 2004, ApJ, 611, 418,
 Bellm, E. C., Kulkarni, S. R., Barlow, T., et al. 2019, PASP, 131, 068003,
 Bellot Rubio, L. R., Ortiz, J. L., & Sada, P. V. 1998, Earth Moon and Planets,
 82, 575,
 Beloborodov, A. M. 2020, ApJ, 896, 142,
 Berger, E., Leibler, C. N., Chornock, R., et al. 2013, ApJ, 779, 18,
 Bertin, E., & Arnouts, S. 1996, A&AS, 117, 393,
 Betzler, A. S., & de Sousa, O. F. 2022, eMeteorNews, 7, 181
 Bochenek, C. D., Ravi, V., Belov, K. V., et al. 2020, Nature, 587, 59,
 Bottke, W. F., & Greenberg, R. 1993, Geophys. Res. Lett., 20, 879,
 Chambers, K. C., Magnier, E. A., Metcalfe, N., et al. 2016, arXiv e-prints,
 arXiv:1612.05560.
 Chen, G., Ravi, V., & Lu, W. 2020, ApJ, 897, 146,
 CHIME/FRB Collaboration, Amiri, M., Andersen, B. C., et al. 2021, ApJS,
 257, 59,
 Corbett, H., Law, N. M., Soto, A. V., et al. 2020, ApJL, 903, L27,
 Drout, M. R., Chornock, R., Soderberg, A. M., et al. 2014, ApJ, 794, 23,
 Ferrari, F., Raducan, S. D., Soldini, S., & Jutzi, M. 2022, PSJ, 3, 177,
 Gaia Collaboration, Brown, A. G. A., Vallenari, A., et al. 2018, A&A, 616,
 A1,
 Gaia Collaboration, Vallenari, A., Brown, A. G. A., et al. 2023, A&A, 674,
 A1,
 Gehrels, N. 1986, ApJ, 303, 336,
 Hardy, L. K., Dhillon, V. S., Spitler, L. G., et al. 2017, MNRAS, 472, 2800,
 Harris, A. W., & Chodas, P. W. 2021, ICARUS, 365, 114452,
 Hiramatsu, D., Berger, E., Metzger, B. D., et al. 2023, ApJL, 947, L28,
 Ho, A. Y. Q., Perley, D. A., Kulkarni, S. R., et al. 2020, ApJ, 895, 49,
 Ivezić, Ž., Kahn, S. M., Tyson, J. A., et al. 2019, ApJ, 873, 111,
 James, C. W., Ekers, R. D., Macquart, J. P., Bannister, K. W., & Shannon,
 R. M. 2019, MNRAS, 483, 1342,
 Jones, D. O., Scolnic, D. M., & Rodney, S. A. 2015, PythonPhot: Simple
 DAOPHOT-type photometry in Python.
 Klebesadel, R. W., Strong, I. B., & Olson, R. A. 1973, ApJL, 182, L85,
 Kojima, Y., Sako, S., Ohsawa, R., et al. 2018, in Society of Photo-Optical
 Instrumentation Engineers (SPIE) Conference Series, Vol. 10709, High
 Energy, Optical, and Infrared Detectors for Astronomy VIII, ed. A. D.
 Holland & J. Beletic, 107091T,
 Lang, D., Hogg, D. W., Mierle, K., Blanton, M., & Roweis, S. 2010, AJ, 139,
 1782,
 Law, N. M., Corbett, H., Galliher, N. W., et al. 2022, PASP, 134, 035003,
 Li, C. K., Lin, L., Xiong, S. L., et al. 2021, Nature Astronomy, 5, 378,

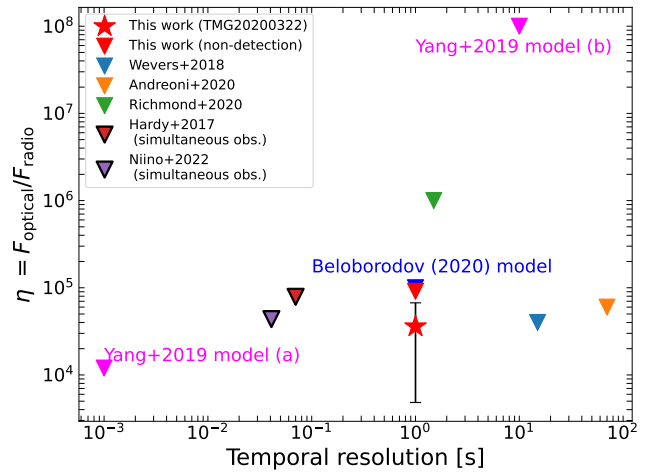


Fig. 14. Comparisons of the fluence ratio η derived from several transient searches which are summarized by Chen et al. (2020) (Wevers et al. 2018; Andreoni et al. 2020; Richmond et al. 2020) as a function of the temporal resolution of each study. We include results from the simultaneous observations of FRBs with optical and radio bands, and model predictions of FRB optical emissions. The error bar of the point (detection case) indicates the 3σ of the power law index of the radio fulence CDF model (James et al. 2019). Alt text: Fluence ratio vs temporal resolution with study markers, upper-limit triangles, a red star for this work, and model labels.

Liakos, A., Bonanos, A. Z., Xilouris, E. M., et al. 2024, *A&A*, 687, A14,

Lipunov, V. M., Kornilov, V. G., Krylov, A. V., et al. 2007, *Astronomy Reports*, 51, 1004,

Lorimer, D. R., Bailes, M., McLaughlin, M. A., Narkevic, D. J., & Crawford, F. 2007, *Science*, 318, 777,

Maehara, H., Shibayama, T., Notsu, Y., et al. 2015, *Earth, Planets and Space*, 67, 59,

Meegan, C. A., Fishman, G. J., Wilson, R. B., et al. 1992, *Nature*, 355, 143,

Megias Homar, G., Meyers, J. M., & Kahn, S. M. 2023, *ApJ*, 950, 21,

Niino, Y., Doi, M., Sako, S., et al. 2022, *ApJ*, 931, 109,

Nir, G., Ofeq, E. O., Ben-Ami, S., et al. 2021a, *MNRAS*, 505, 2477,

Nir, G., Ofeq, E. O., & Gal-Yam, A. 2021b, *Research Notes of the American Astronomical Society*, 5, 27,

Ochsenbein, F., Bauer, P., & Marcout, J. 2000, *A&AS*, 143, 23,

Ohsawa, R., Hirota, A., Morita, K., et al. 2020, *Planet. Space Sci.*, 194, 105011,

Ortiz, J. L., Sada, P. V., Bellot Rubio, L. R., et al. 2000, *Nature*, 405, 921,

Oshikiri, K., Tanaka, M., Tominaga, N., et al. 2024, *MNRAS*, 527, 334,

Petroff, E., Johnston, S., Keane, E. F., et al. 2015, *MNRAS*, 454, 457,

Petroff, E., Barr, E. D., Jameson, A., et al. 2016, *PASA*, 33, e045,

Platts, E., Weltman, A., Walters, A., et al. 2019, *Phys. Rep.*, 821, 1,

Prentice, S. J., Maguire, K., Smartt, S. J., et al. 2018, *ApJL*, 865, L3,

Racusin, J. L., Karpov, S. V., Sokolowski, M., et al. 2008, *Nature*, 455, 183,

Rau, A., Ofeq, E. O., Kulkarni, S. R., et al. 2008, *ApJ*, 682, 1205,

Richmond, M. W., Tanaka, M., Morokuma, T., et al. 2020, *PASJ*, 72, 3,

Rykoff, E. S., Aharonian, F., Akerlof, C. W., et al. 2005, *ApJ*, 631, 1032,

Sako, S., Ohsawa, R., Takahashi, H., et al. 2018, in *Society of Photo-Optical Instrumentation Engineers (SPIE) Conference Series*, Vol. 10702, *Ground-based and Airborne Instrumentation for Astronomy VII*, ed. C. J. Evans, L. Simard, & H. Takami, 107020J,

Shappee, B. J., Prieto, J. L., Grupe, D., et al. 2014, *ApJ*, 788, 48,

Smith, K. W., Smartt, S. J., Young, D. R., et al. 2020, *PASP*, 132, 085002,

Sokołowski, M., Małek, K., Piotrowski, L. W., & Wrochna, G. 2010, *Advances in Astronomy*, 2010, 463496,

Stetson, P. B. 1987, *PASP*, 99, 191,

Suggs, R., Moser, D., Cooke, W., & Suggs, R. 2014, *Icarus*, 238, 23,

Tanaka, M., Takahashi, I., Yoshida, N., et al. 2025, *ApJ*, 994, 175,

Thornton, D., Stappers, B., Bailes, M., et al. 2013, *Science*, 341, 53,

Tingay, S., & Joubert, W. 2021, *PASA*, 38, e001,

Tominaga, N., Niino, Y., Totani, T., et al. 2018, *PASJ*, 70, 103,

Tony, J. L., Denneau, L., Heinze, A. N., et al. 2018, *PASP*, 130, 064505,

Vestrand, W. T., Wozniak, P. R., Wren, J. A., et al. 2005, *Nature*, 435, 178,

Wevers, T., Jonker, P. G., Hodgkin, S. T., et al. 2018, *MNRAS*, 473, 3854,

Xilouris, E. M., Bonanos, A. Z., Bellas-Velidis, I., et al. 2018, *A&A*, 619, A141,

Yamagata, T., & Maehara, H. 1986, *Ap&SS*, 118, 459,

Yang, Y.-P., Zhang, B., & Wei, J.-Y. 2019, *ApJ*, 878, 89,